Calhoun: The NPS Institutional Archive

DSpace Repository

Faculty and Researchers | Faculty and Researchers' Publications

2018-02

SAR Focus Theory of Complicated Range Migration Signatures Due to Moving Targets

Garren, David Alan

Garren, David Alan. "SAR Focus Theory of Complicated Range Migration Signatures Due to Moving Targets." IEEE Geoscience and Remote Sensing Letters (2018). http://hdl.handle.net/10945/59009

This publication is a work of the U.S. Government as defined in Title 17, United States Code, Section 101. Copyright protection is not available for this work in the United States.

Downloaded from NPS Archive: Calhoun

http://www.nps.edu/library

Calhoun is the Naval Postgraduate School's public access digital repository for research materials and institutional publications created by the NPS community. Calhoun is named for Professor of Mathematics Guy K. Calhoun, NPS's first appointed -- and published -- scholarly author.

Dudley Knox Library / Naval Postgraduate School
411 Dyer Road / 1 University Circle
Monterey, California USA 93943

SAR Focus Theory of Complicated Range Migration Signatures Due to Moving Targets

David Alan Garren, *Senior Member, IEEE*

***Abstract*— Recent studies have revealed that the residual range migration effects of synthetic aperture radar (SAR) imagery smears induced by moving targets can exhibit complicated shapes that are not limited to that of parabolas. This letter demonstrates that automatic focusing methods can remove such range migration effects by estimating and compensating for phase errors directly in the radar video phase history domain. This approach is validated using measured Ku-band SAR clutter data containing buildings and foliage.**

***Index Terms*— Moving target imaging, radar signatures, residual range migration, synthetic aperture radar (SAR).**

I. Introduction

MOBILE targets in synthetic aperture radar (SAR) imagery can be moving during the collection. Unfortunately, the corresponding signatures are often smeared beyond recognition. Numerous research works have examined methods [1]–[5] for target focusing. Often these methods compensate for defocus only in the radar cross-range direction. However, SAR moving target signatures often exhibit gently curved parabolic or hyperbolic shapes [6].

Jao [6] developed methods for refocusing the curved signatures of constant velocity targets. This signature bowing is related to the range migration algorithm (RMA) that is applied for focusing stationary scenes [7]. Rahman [8] investigated RMA for focusing such constant velocity target smears. However, recent methods [9]–[13] predict the complicated 2-D range migration smearing due to targets with nonuniform motion, as with braking maneuvers.

This letter investigates methods that automatically generate focused imagery of targets that are moving with arbitrary translational profiles that are not restricted to be low-order parametric models, as with constant velocity or acceleration. One approach is to adapt the phase gradient autofocus (PGA) of Wahl *et al.* [14] and Jakowatz *et al.* [15] that focus stationary scenes. The range migration errors remaining after stationary scene autofocus are insignificant and thus do not benefit from the current methods. However, the residual range migration of moving targets can be important [6].

The current approach performs the estimation and compensation processes directly to the video phase history (VPH) data and thus has broad utility. Specifically, it applies if the transmitter and the receiver are colocated or separated. It applies regardless of their flight paths. It is applicable to both stripmap and spotlight SAR. It also applies for all types of SARs, including RMA, chirp scaling algorithm, polar format algorithm (PFA), and backprojection algorithm (BPA) [16], [17].

Section II defines the error estimation process, and Sections III and IV describe the radar data and autofocus results, respectively. The conclusions are given in Section V.

Manuscript received December 8, 2017; revised January 23, 2018; accepted January 25, 2018. Date of publication February 12, 2018; date of current version March 23, 2018.

The author is with the Department of Electrical and Computer Engineering, Naval Postgraduate School, Monterey, CA 93943 USA (e-mail: dagarren@nps.edu).

Color versions of one or more of the figures in this letter are available online at http://ieeexplore.ieee.org.

Digital Object Identifier 10.1109/LGRS.2018.2799818

II. Error Estimation

The analysis herein uses a data-driven approach in which the radar VPH data are used to estimate the changes in the bistatic range of a moving target relative to the radar system. These distance changes ultimately yield undesired phase errors that give an unfocused target image. Define the bistatic range s to be one-half of the summed distance from the transmitter to a particular target scattering center and back to the receiver. The one-half is included so that s reduces to the standard range for monostatic SAR.

Consider two successive complex-valued bistatic range profile measurements. Assume that a particular waveform along the synthetic aperture is indexed by n. Define the scalar $\{r_n\}$ to be equal to one-half of the unknown two-way distance for waveform n to travel from the transmitter to a target scattering center and back to the receiver. Then, $\{r_{n+1}\}$ is the unknown bistatic range distance for the next waveform $n+1$. Thus, two successive measurement profiles $g(s)$ have the form

$$g_1(s) \equiv g(s|r_n), \quad g_2(s) \equiv g(s|r_{n+1}). \tag{1}$$

The notation | indicates that $\{r_n\}$ and $\{r_{n+1}\}$ are unknown parameters that affect the particular profile in s in (1).

For each waveform n, the range s and the unknown errors $\{r_n\}$ and $\{r_{n+1}\}$ are defined relative to a particular bistatic range reference $R_{n,0}$. The value of $R_{n,0}$ is determined by the selected radar motion compensation methodology. For spotlight SAR, $R_{n,0}$ is the bistatic range to a fixed ground reference point at which the radar transmission and reception mainbeams are aimed during the collection process.

It is desired to develop a data-driven methodology for estimating the unknown increments $\{\Delta r_n\}$ in the target bistatic range distance between adjacent waveforms

$$\Delta r_n \equiv r_{n+1} - r_n. \tag{2}$$

The corresponding values of s for a given moving target scattering center at the successive waveforms are given by

$$s_n = r_n, \quad s_{n+1} = r_n + \Delta r_n. \tag{3}$$

U.S. Government work not protected by U.S. copyright.

This error model is straightforward but is included for clarity.

A given scattering center indexed by i is characterized by a complex-valued strength σ_i. Define the waveform envelope function $\tilde{p}(t)$ to be a smooth function in terms of the fast time t. Also assume that f_0 is the center frequency of the narrowband transmitted waveform pulse. Denote the function $\tilde{P}(f)$ to be the Fourier transform of $\tilde{p}(t)$ in terms of the fast-time frequency f. A modulated chirp waveform with bandwidth Δ_f is often a practical choice (see [18]).

Next, the processing includes the inverse Fourier transform of measured VPH data, accounting for the narrow bandwidth of the waveform spectrum compared with that of the carrier frequency f_0. Then, a frequency down-conversion to baseband is performed, yielding the following signal model of the compressed narrowband waveform that is reflected from a give target scattering center:

$$\tilde{g}_i(t) = \sigma_i \tilde{p}\left(t - \frac{2r_n}{c}\right) \exp\left(-\frac{j4\pi f_0 r_n}{c}\right). \tag{4}$$

Here, c is the speed of light, and $j = \sqrt{-1}$. This model is used extensively in the analysis of SAR (see [14], [15], [19]).

It is convenient to transform from the time variable t to the spatial variable $s \equiv ct/2$. Thus, (4) becomes

$$g_i(s \mid r_n) = \sigma_i p(s - r_n) \exp\left(-\frac{j4\pi r_n}{\lambda_0}\right) \tag{5}$$

using the wavelength $\lambda_0 = c/f_0$ and $p(s) \equiv \tilde{p}(2s/c)$.

Consider the presence of an unmodeled target motion that induces a bistatic range error Δr_n, so that (5) becomes

$$g_i(s \mid r_n + \Delta r_n) = \sigma_i p(s - r_n - \Delta r_n) \exp\left(-\frac{j4\pi\{r_n + \Delta r_n\}}{\lambda_0}\right). \tag{6}$$

It is reasonable to assume that waveform pulse envelope is smooth and of finite duration. Thus, the approximation $p(s - \Delta r_n) \cong p(s)$ can be applied, provided that Δr_n is much smaller than the compressed pulsewidth. Then, (6) can be approximated as

$$g_i(s \mid r_n + \Delta r_n) \cong \sigma_i p(s - r_n) \exp\left(-\frac{j4\pi r_n}{\lambda_0}\right) \exp\left(-\frac{j4\pi \Delta r_n}{\lambda_0}\right). \tag{7}$$

Therefore, the motion-induced range error Δr_n yields a phase error that is applied to the VPH measurements

$$g_i(s \mid r_n + \Delta r_n) \cong g_i(s \mid r_n) \exp\left(-\frac{j4\pi \Delta r_n}{\lambda_0}\right). \tag{8}$$

Thus, the signal model for the VPH data is

$$g_{1,p} = \beta_p + q_{1,p} \tag{9}$$

$$g_{2,p} = \beta_p \exp(-j2\pi\rho_c \Delta r_n) + q_{2,p} \tag{10}$$

in terms of the central spatial frequency $\rho_c \equiv 2/\lambda_0$. The separate subscripts 1 and 2 are used within the additive white Gaussian noise (AWGN) terms in (9) and (10), which are assumed to be independent and identically distributed.

The phase error arising from target reflections corresponding to successive radar waveforms along the synthetic aperture is

$$\Delta\varphi_n \equiv -2\pi\rho_c \Delta r_n. \tag{11}$$

Then, the signal model equations become

$$f_p = \beta_p + q_{1,p}, \quad g_p = \beta_p \exp(j\Delta\varphi_n) + q_{2,p}. \tag{12}$$

This form is basically the same as that used in PGA in [14] and [15]. However, the present methodology applies these techniques directly to VPH data rather than image data. The interference product data in VPH domain are

$$\gamma_p = f_p^* g_p. \tag{13}$$

Maximum-likelihood techniques [15] yield the nonparametric phase difference error estimate

$$\widehat{\Delta\varphi}_n = \angle\left[\sum_{p=1}^{P} \gamma_p\right] \tag{14}$$

wherein $\angle$ is the unwrapped phase angle. Thus, (11) implies that the final distance difference variation estimate is

$$\widehat{\Delta r}_n = -\frac{\widehat{\Delta\varphi}_n}{2\pi\rho_c}. \tag{15}$$

The estimate of the nonparametric distance variation $\hat{r}_n$ is computed by integrating $\widehat{\Delta r}_n$ along the synthetic aperture via n. The constant of integration is set so that the mean distance variation is zero. Thus, the refocused target image is not shifted in cross range relative to the input smear. This constant is effectively absorbed into the complex-valued β_p.

The resulting error-compensated VPH data have the form

$$H_n(\rho) = F_n(\rho) \exp(j2\pi\rho\hat{r}_n). \tag{16}$$

The inverse Fourier transform of $H_n(\rho)$, i.e.,

$$h_n(s) \equiv \int d\rho H_n(\rho) \exp(j2\pi\rho s) \tag{17}$$

is applied to give the error-compensated range-compressed VPH measurement data $h_n(s)$, wherein the unmodeled distance variation errors have been removed. Then, $h_n(s)$ can be input into standard SAR image formation algorithms, such as PFA, RMA, BPA, etc., to yield focused target imagery.

III. Radar Data

The current approach is valid for any SAR processing, since the error estimation and compensation is performed directly on the VPH data prior to image formation. For brevity, examples are presented only for a monostatic broadside geometry and PFA image formation. The investigation involving a large span of measurement geometries and image formation algorithms is beyond the current scope and is deferred for future work.

The formulation of in [9] and [11]–[13] is applied to generate the simulated SAR signature of a moving target. The geometry for the selected example is shown in Fig. 1(a). The radar has a rightward-pointing mainbeam and a constant and level flight path. The radar parameters include a speed of $V_0 = 71.3763$ m/s, a ground range of $X_0 = 2.914$ km, and an altitude of $Z_0 = 1.496$ km. The radar center frequency is

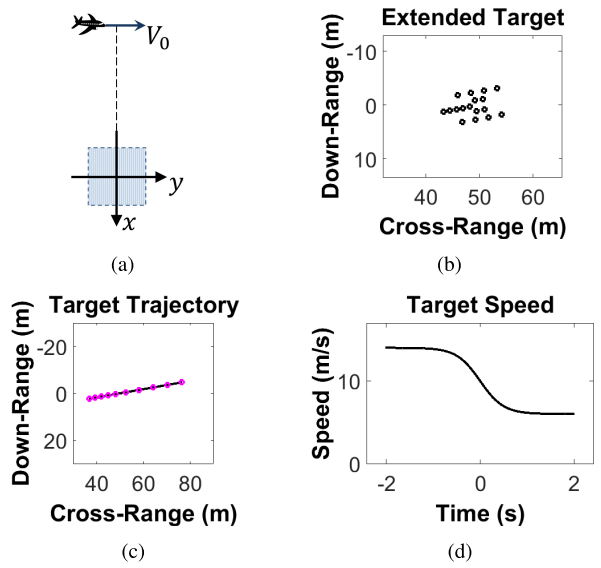

Fig. 1. Collection geometry and true target motion. (a) Broadside collection with a rightward-pointing radar mainbeam. (b) Target composed of point scattering centers. (c) Target trajectory in the ground plane, with circles at 0.5-s intervals. (d) Corresponding target speed profile.

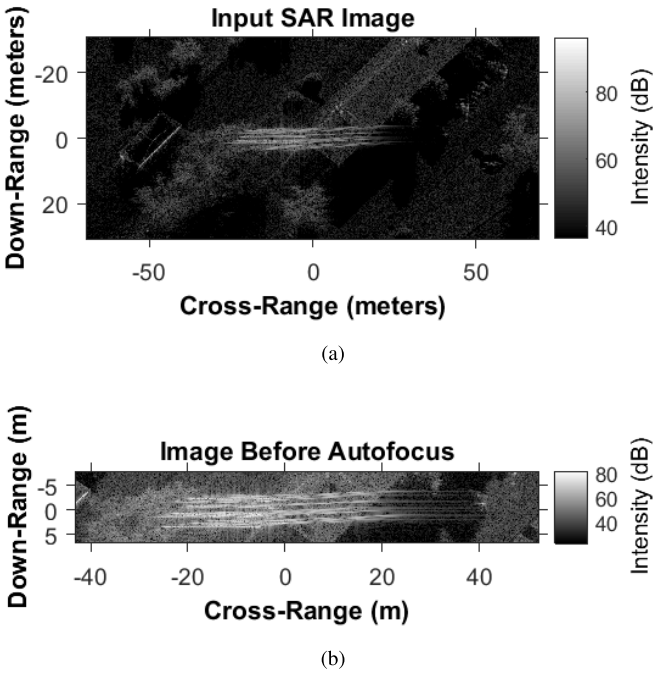

Fig. 2. Moving target smear containing range migration corresponding to the true target motion of Fig. 1 has been combined with measured Ku-band SAR data. (a) Original image. (b) Tighter ROI.

$f_c = 16.8$ GHz, the bandwidth is 1.6593 GHz, and the total SAR coherent processing interval is $T_0 = 4.034$ s.

Fig. 1(b) presents a target that is composed of a selected set of idealized scattering centers. These point reflectors are translated according to a constant heading trajectory with a braking maneuver, as presented in Fig. 1(c). The corresponding speed profile in time is shown in Fig. 1(d).

Fig. 2(a) shows the moving target smear corresponding to the true target motion of Fig. 1, which has been combined with measured Ku-band SAR data [20]. The presence of both human-made and natural clutter is evident. The phase has been retained in combining the simulated moving target data with the measured data in order to examine the robustness of the subject VPH-based autofocus of moving targets to the effects of clutter and noise. Furthermore, the radar parameters of the simulated data are identical to that of the measured clutter. This strategy is useful since the phase errors induced by target motion are known exactly and thus provides an accurate means of comparison. In addition, scripted data collections are costly and beyond the scope of the present theoretical work.

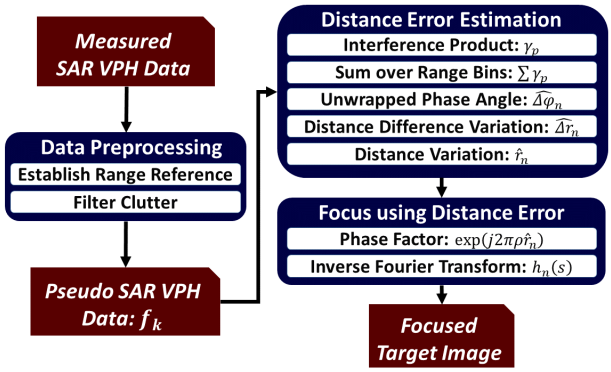

Fig. 3. Functional block diagram for the subject VPH-based moving target autofocus processing.

IV. Moving Target Autofocus Results

A diagram for the current moving target autofocus methodology is given in Fig. 3. Outputs at various stages are provided in Figs. 4 and 5 to clarify the functionality.

The moving target autofocus approach developed herein is applied to pseudo-VPH data that are generated using the complex-valued image chip within a selected region of interest (ROI). Specifically, the ROI that surrounds a target smear of interest is forward-projected to generate pseudoradar return data, as described in [21]. Then, these data are processed as if they were the original VPH measurements within the remainder of the estimation and refocus processing. This approach enables the masking and removal of the effects of most clutter and other targets, both stationary and moving. Specifically, forward projection processing is applied to a given ROI in order to generate pseudo-VPH data, which contain the motion-induced smear, but with the majority of the residual clutter and other targets excised.

This approach assumes that initial screening is applied to detect moving target smears within the full SAR image (e.g., shear averaging [3]). Specifically, the ROI for each detected moving target smear is extracted and refocused separately. The ROI extraction can be performed automatically via algorithmic processing or through the intervention of a human operator. The resulting ROI was extracted from the larger image chip of Fig. 2(a). Range migration defocus effects are evident in Fig. 2(b), wherein the smearing toward the right side is not oriented purely horizontally.

The complex-valued summation of the moving target smear with the measured Ku-band SAR imagery enables separate computations for the integrated image energies of

both contributions, yielding the target signal to clutter-plus-noise ratio (SCNR). The ROI selection process increases the SCNR from 3.4010 dB for Fig. 2(a) to 19.3352 dB for Fig. 2(b).

Fig. 4(a) gives the complex phase angle of the interference product data of (13). The phase angle values lie between $-\pi$ and π, wherein a magnitude mask suppresses values below a minimum threshold. The examination reveals that many scattering centers in the true target of Fig. 1(b) cause the many scattering bands in the range profile to interfere and blend with one another. If there were only a few scattering centers, then one could discern individual bands in this plot.

The spatial position of zero phase is selected to correspond to the center of the ROI image chip of Fig. 2(a). This selection is effectively equivalent to the resetting of the motion compensation point of the pseudo-VPH data to be the ROI center. Such an approach is used in the current processing, as evident with the approximately horizontal range–time plots of Fig. 4(a). If zero phase had been selected far from the ROI, then these lines would exhibit a large nonzero slope.

Fig. 4(b) shows the distance difference variation obtained summing the interference product data of (14). The shadowing (i.e., light versus dark) of the 2-D phase angle plots of Fig. 4(a) corresponds with the values (i.e., peaks versus valleys) of the 1-D phase angle data of Fig. 4(b).

Fig. 4(b) also reveals that the estimate of the distance difference variation is relatively accurate for most waveform indices, except near the beginning and end of the synthetic aperture. This effect is expected since some noise and clutter remains within the selected ROI, although the majority is excised. These competing effects are more problematic in regions wherein the smear intensity diminishes and appears to vanish into the background, which often corresponds to the beginning and end of the synthetic aperture [11]. Thus, this decreased target SCNR degrades the estimation accuracy of the distance difference variation of (14) near the beginning and end of the collection.

Integration of the distance difference variation of Fig. 4(b) along the synthetic aperture yields the distance variation function shown in Fig. 4(c). Fig. 4(c) shows accurate agreement with truth for most of the synthetic aperture, except near the beginning and end of the collection. This result also follows from the decreased target smear intensity at the beginning and end of the signature contour.

Recall from Section II that Δr_n is assumed to be much smaller the compressed pulsewidth. Note that Δr_n, as plotted in Fig. 4(b), corresponds to the residual range migration between any two consecutive transmission waveforms along the synthetic aperture. Thus, the total residual range migration r_n, as shown in Fig. 4(c), integrates perhaps thousands or more of such adjacent waveform pairs along the full synthetic aperture and can yield a total range cell migration of several imagery pixels. The differences in the vertical scales of Fig. 4(b) and (c) are consistent with this fact.

For the case of exactly zero noise and clutter, the estimated curves of Fig. 4(b) and (c) visually yield identical curves with that corresponding to the truth profiles when compared on the current plotting scales, even at the beginning and end of the synthetic aperture. These results are omitted for brevity.

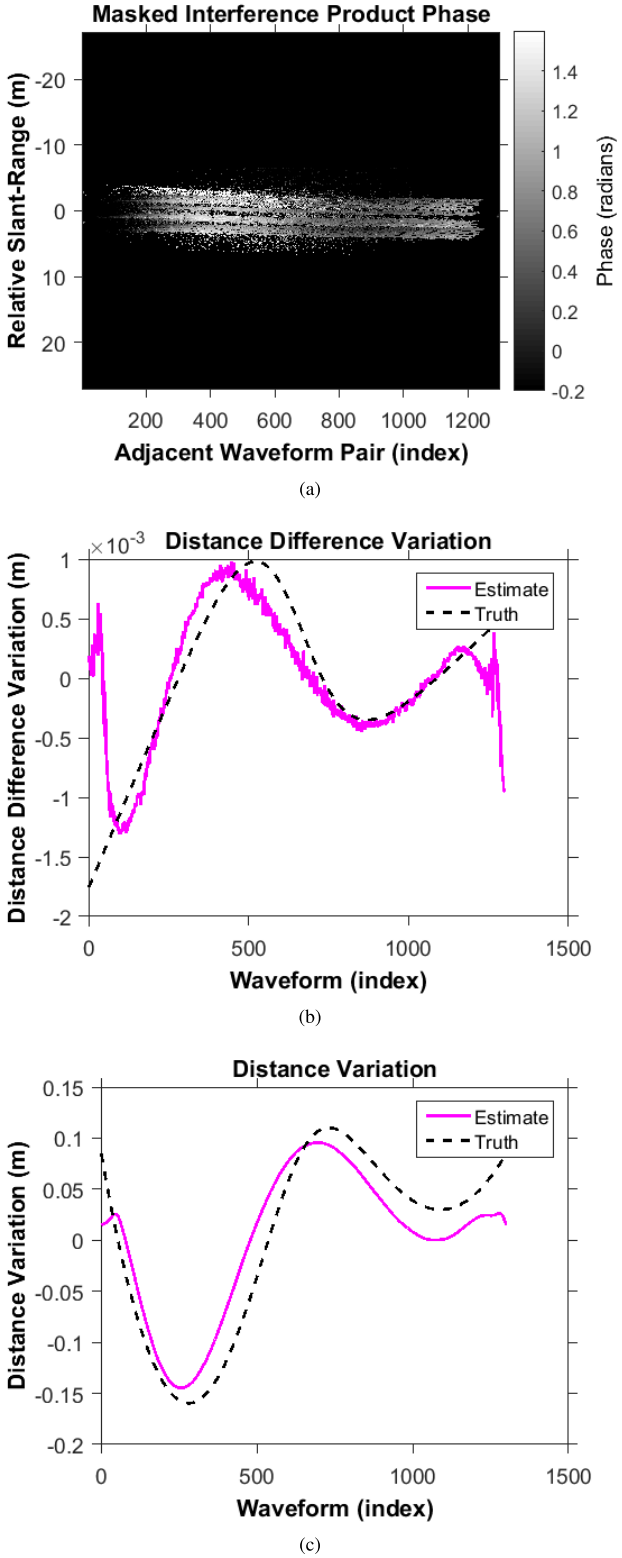

Fig. 4. Processing details. (a) Complex phase angle of the interference product data of (13) with a magnitude mask. (b) Estimated and truth curves for the corresponding distance difference variation. (c) Estimated and truth curves for the corresponding distance variation.

Finally, Fig. 5 gives the focused SAR image resulting from the use of the estimated phase error, which reveals

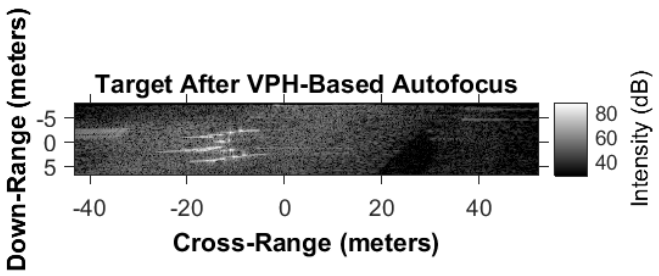

Fig. 5. Focused target image obtained after the subject moving target refocus methodology is applied to the ROI of Fig. 2(b), showing good agreement with the truth of Fig. 1(b).

good agreement with Fig. 1(b). Image regions with seemingly residual target defocus, as with the top left, are due to neighboring building clutter that has become defocused during the automatic focusing of the moving target.

The spatial mask ROI filtering provides a partial mechanism for mitigating the deleterious effects of stationary clutter. To understand this concept, consider that each individual pixel within the input imagery can contain all of the following: 1) defocused target smearing; 2) buildings, foliage, and other stationary clutter; and 3) noise. Of course, the brightest parts of the moving target smear should be included within the ROI processing, since the SCNR is high for such image pixels.

In contrast, beyond the left and right visible cross-range boundaries of the smear, the moving target SCNR is relatively low, so the inclusion of such image pixels into the processing can degrade the quality of the error estimate. Likewise, the target SCNR is also small beyond the upper and lower down-range boundaries of the smear. If one includes these low SCNR imagery pixels into the error estimation processing, then the overall target refocus quality is degraded.

V. Conclusion

The theory presented herein demonstrates the viability of compensating for range migration effects in refocusing moving target signature smears. This analysis also confirms that PGA estimation techniques can be applied to VPH data prior to image formation in order to affect this outcome.

The importance of this methodology is that it refocuses the original mover smear as if the target were stationary. That is, the motion-induced target signatures can exhibit undesired range migration over multiple range resolution cells. The current technique effectively integrates this range-smeared image energy so that the residual range migration is removed.

It is possible that there does not exist a single algorithm that gives the best focus results for all moving target smears. The current methodology gives accurate target refocus for maneuvering targets in a low-to-moderate clutter environment. Target refocus degrades as the SCNR falls below 10 dB and becomes poor if the SCNR is lower than 0 dB. The generation of an optimal mover target refocus algorithm for all cases is reserved for future work.

Acknowledgment

DoD Distribution Statement A: Unlimited Distribution. The views expressed in this document are those of the author and do not reflect the official policy or position of the Department of Defense or the U.S. Government. Measured complex-valued Ku-band MiniSAR data provided courtesy of Sandia National Laboratories, Airborne ISR [20].

References

[1] R. K. Raney, "Synthetic aperture imaging radar and moving targets," *IEEE Trans. Aerosp. Electron. Syst.*, vol. AES-7, no. 3, pp. 499–505, May 1971.

[2] R. P. Perry, R. C. DiPietro, and R. Fante, "SAR imaging of moving targets," *IEEE Trans. Aerosp. Electron. Syst.*, vol. 35, no. 1, pp. 188–200, Jan. 1999.

[3] J. R. Fienup, "Detecting moving targets in SAR imagery by focusing," *IEEE Trans. Aerosp. Electron. Syst.*, vol. 37, no. 3, pp. 794–809, Jul. 2001.

[4] D. Cristallini, D. Pastina, F. Colone, and P. Lombardo, "Efficient detection and imaging of moving targets in SAR images based on chirp scaling," *IEEE Trans. Geosci. Remote Sens.*, vol. 51, no. 4, pp. 2403–2416, Apr. 2013.

[5] B. D. Rigling, "Image-quality focusing of rotating SAR targets," *IEEE Geosci. Remote Sens. Lett.*, vol. 5, no. 4, pp. 750–754, Oct. 2008.

[6] J. K. Jao, "Theory of synthetic aperture radar imaging of a moving target," *IEEE Trans. Geosci. Remote Sens.*, vol. 39, no. 9, pp. 1984–1992, Sep. 2001.

[7] R. H. Stolt, "Migration by Fourier transform," *Geophysics*, vol. 43, no. 1, pp. 23–48, 1978.

[8] S. Rahman, "Focusing moving targets using range migration algorithm in ultra wideband low frequency synthetic aperture radar," M.S. thesis, Dept. Elect. Eng., Blekinge Inst. Technol., Karlskrona, Sweden, Jun. 2010.

[9] D. A. Garren, "Smear signature morphology of surface targets with arbitrary motion in spotlight synthetic aperture radar imagery," *IET Radar, Sonar Navigat.*, vol. 8, no. 5, pp. 435–448, Jun. 2014.

[10] K. Duman and B. Yacici, "Moving target artifacts in bistatic synthetic aperture radar images," *IEEE Trans. Comput. Imag.*, vol. 1, no. 1, pp. 30–43, Mar. 2015.

[11] D. A. Garren, "Theory of two-dimensional signature morphology for arbitrarily moving surface targets in squinted spotlight synthetic aperture radar," *IEEE Trans. Geosci. Remote Sens.*, vol. 53, no. 9, pp. 4997–5008, Sep. 2015.

[12] D. A. Garren, "Signature morphology effects of squint angle for arbitrarily moving surface targets in spotlight synthetic aperture radar," *IEEE Trans. Geosci. Remote Sens.*, vol. 53, no. 11, pp. 6241–6251, Nov. 2015.

[13] D. A. Garren, "SAR ground plane mover signatures for nonzero radar ascent," *IEEE Trans. Aerosp. Electron. Syst.*, vol. 53, no. 3, pp. 2214–2220, Oct. 2017.

[14] D. E. Wahl, P. H. Eichel, D. C. Ghiglia, and C. V. Jackowatz, Jr., "Phase gradient autofocus—A robust tool for high resolution SAR phase correction," *IEEE Trans. Aerosp. Electron. Syst.*, vol. 30, no. 3, pp. 827–834, Jul. 1994.

[15] C. V. Jakowatz, Jr., D. E. Wahl, P. H. Eichel, D. C. Ghiglia, and P. A. Thompson, *Spotlight-Mode Synthetic Aperture Radar: A Signal Processing Approach*. Norwell, MA, USA: Kluwer, 1996.

[16] A. F. Yegulalp, "Fast backprojection algorithm for synthetic aperture radar," in *Proc. IEEE Radar Conf.*, Apr. 1999, pp. 60–65.

[17] L. M. H. Ulander, H. Hellsten, and G. Stenström, "Synthetic-aperture radar processing using fast factorized back-projection," *IEEE Trans. Aerosp. Electron. Syst.*, vol. 39, no. 3, pp. 760–776, Jul. 2003.

[18] M. Soumekh, *Synthetic Aperture Radar Signal Processing With MATLAB Algorithms*. New York, NY, USA: Wiley, 1999.

[19] R. J. Sullivan, *Radar Foundations for Imaging and Advanced Concepts*. Raleigh, NC, USA: SciTech, 2004.

[20] Sandia National Laboratories. (2017). *Complex SAR Data*. [Online]. Available: http://www.sandia.gov/radar/complex-data/

[21] M. Martorella, E. Giusti, F. Berizzi, A. Bacci, and E. D. Mese, "ISAR based technique for refocusing non-cooperative targets in SAR images," *IET Radar, Sonar Navigat.*, vol. 6, no. 5, pp. 332–340, 2012.